THIS IS AN EARLY ACCESS ARTICLE.
This article has been accepted for publication in a future issue of this journal,
but has not been fully edited. Content may change prior to final publication.

BULLETIN OF THE POLISH ACADEMY OF SCIENCES
TECHNICAL SCIENCES
DOI: 10.24425/bpasts.2027.7725

Robust Fractional-Order Control of Manipulators Based on SMC-ADRC Dynamic Coordination and Intelligent Optimization

Yifang WEN[1, 2], Renzhong WANG[1, 2*], Ting HUANG[1, 2]

[1] School of Mechanical and Electrical Engineering, Suzhou Polytechnic University, 215000 Suzhou, China
[2] Robotics and Intelligent Equipment Engineering Research Center of Jiangsu Province, Suzhou Polytechnic University, 215000 Suzhou, China

Abstract. To address the limitations posed by model uncertainties and the constraints of single control methods in high-precision trajectory tracking of manipulators, this paper proposes a novel dynamic coordination strategy integrating fractional-order sliding mode control (FOSMC) and fractional-order active disturbance rejection control (FOADRC). A super-twisting algorithm-based FOSMC is designed to ensure robustness and suppress chattering, while a FOADRC is developed to estimate and compensate for disturbances. Key parameters of the FOADRC are systematically tuned using a particle swarm optimization algorithm. An adaptive S-function-based dynamic weighting mechanism is introduced to smoothly adjust the outputs of the two controllers according to real-time tracking error, thereby achieving effective fusion of rapid convergence under large errors and high steady-state accuracy under small errors. Simulation results on a two-degree-of-freedom manipulator demonstrate that, compared to using FOSMC or FOADRC alone, the proposed collaborative strategy significantly improves tracking performance: the root mean square error is reduced by over 52%, the convergence rate is increased by approximately 23.5%, and the smoothness of the control input is enhanced with a variance reduction exceeding 53%. This study validates the effectiveness of the dynamic collaborative mechanism in realizing high precision, rapid response, and strong robustness in complex manipulator control.

Key words: Manipulator; Fractional order control; Collaborative control; Optimization algorithm; Trajectory tracking

1. INTRODUCTION

The manipulator is a multi-body system composed of multiple links connected in series through joints [1-2]. Its dynamics exhibit strong nonlinearity and coupling, making it difficult to establish an accurate mathematical model solely from physical principles. The unmodeled dynamics such as joint friction, transmission clearance, link flexibility and so on, which are common in the system, further aggravate the model mismatch. At the same time, in the actual working environment, the manipulator also needs to deal with the load change, external random disturbance and the rapid change of task instructions [3-4]. Model uncertainties, internal parameter perturbations, and external unknown disturbances often coexist and intertwine. This makes traditional model-based control methods, e.g., computational torque method, perform poorly in practical applications. Moreover, their performance is extremely sensitive to model accuracy and lacks robustness.

Therefore, developing advanced control theory that does not rely on an accurate plant model [5-6] has become crucial. Such theory can actively suppress system uncertainties, thereby improving manipulator performance and expanding its application boundaries [7-8]. The core challenge is that an ideal control strategy must simultaneously handle several contradictory requirements. First, it needs strong robust stability to ensure safety under large-scale uncertainties and disturbances. Second, it must exhibit excellent dynamic response speed to reduce tracking lag when following rapidly changing trajectories. Third, it should achieve high steady-state accuracy without overshoot and maintain smooth control output near the target trajectory. This avoids actuator wear and ensures final operation quality [9-10].

In order to overcome the robustness problem of manipulator control, sliding mode control and active disturbance rejection control algorithm are widely used in the existing research [11-12]. The core idea of sliding mode control is to design a specific sliding mode surface and construct a control law to drive the system state to reach and maintain on the surface in a finite time. However, the disadvantages of its classical form are particularly obvious in the specific object of the manipulator: in order to achieve the ideal sliding mode, the control law must include high-frequency switching term, which directly leads to the chattering of the control torque [13-14]. In the actual manipulator system, this kind of chattering can not be perfectly

*e-mail: wrz91811@126.com

This article has been accepted for publication in a future issue of this journal, but has not been fully edited. Content may change prior to final publication.

reproduced by physical actuators such as motors, but also will cause a series of negative effects. In order to suppress chattering, improved methods such as high-order sliding mode and terminal sliding mode are proposed. The core of these methods is to smooth the control signal or accelerate the convergence process while maintaining robustness. However, how to completely eliminate the impact of chattering on accuracy in the high-speed and high acceleration motion of the manipulator is still a difficulty in practice.

Active disturbance rejection control (ADRC) does not rely on obtaining accurate and complex nonlinear differential equations of the manipulator. This idea effectively reduces the dependence on system parameter identification and fits the application scenario of manipulator. Through feed-forward compensation, the controller can output a smoother torque command. However, its performance bottleneck lies in the expansion of the state observer itself, and the selection of observer bandwidth is fundamentally contradictory in the control of manipulator. Setting a high bandwidth allows quick disturbance tracking. However, it inevitably amplifies measurement noise from the joint encoder, causing sharp fluctuations in the estimated value and introducing new interference [15 - 16]. Conversely, adopting a low bandwidth ensures smooth estimation. But during high-speed, large-scale motions, the observer cannot capture rapid changes in internal coupling forces in time. This results in compensation lag, as well as obvious tracking phase errors and dynamic lag. This contradiction is particularly prominent in the task of short working cycle and dramatic movement changes of the manipulator [17-18].

In order to further fine tune the dynamic performance of the above two methods on the manipulator system, fractional calculus theory is introduced into the design framework of the controller [19-20]. In fractional-order sliding mode control, designing an appropriate fractional-order sliding surface and selecting suitable orders can optimize damping characteristics during the rapid approach to the desired trajectory from the initial position. This accelerates convergence while reducing angular overshoot. Consequently, it effectively avoids violent shaking of the manipulator during starting, braking, or trajectory inflection. In fractional order active disturbance rejection control, the fractional order observer or feedback law can be used to configure the phase characteristics of the closed-loop system more flexibly, so as to improve the stability margin of the system in the face of model uncertainty [21-22].

Although the performance of both methods has been improved through fractional order improvement, its inherent limitations still exist when applied to complex manipulator systems as a single architecture [23-24]. Through in-depth analysis, it can be found that most of the existing collaboration strategies are static or open-loop simple superposition. They usually use a fixed combination coefficient or hard switching between the two modes based on a preset either or error threshold. This coordination mechanism fails to deeply match the periodic dynamic requirements of the trajectory tracking task of the manipulator. Both controllers involve many key parameters, including sliding mode surface parameters, fractional orders, observer bandwidth, and feedback gains. Their synergistic effect heavily depends on the proper coordination and matching of these parameters [25-26]. At present, there is no systematic framework to jointly optimize the parameter set of the whole cooperative system for the overall control performance index of the manipulator, so as to achieve the global performance optimization.

In response to the research gap mentioned above, this paper proposes a dynamic collaborative control strategy for a robotic arm based on FOSMC and FOADRC, and carries out systematic design and verification work. The main research content and innovative points of this article are as follows. (1) A fast terminal sliding mode surface that integrates fractional order integral and terminal attractor is designed, and a switching control law is designed using the super-twisting algorithm. This effectively suppresses the chattering of traditional sliding mode control while ensuring finite time convergence and strong robustness. (2) A fractional order linear extended state observer is designed to estimate and compensate for the system's total disturbances in real time. The particle swarm optimization algorithm is introduced, which takes the comprehensive tracking error and control energy consumption as performance indicators to automatically optimize the optimal parameter set of the fractional order PD controller and observer. (3) A dynamic weight allocation mechanism is designed based on S-shaped function. This mechanism can smoothly and continuously adjust the weights of FOSMC and FOADRC outputs in the overall control law based on the absolute value of joint tracking error.

This article is divided into five chapters, arranged as follows: Chapter 1 is the introduction, which elaborates on the research background, significance, current situation, and work of this article. Chapter 2 establishes a dynamic model of a robotic arm based on Lagrange method. Chapter 3 elaborates in detail on the design of sliding mode controller based on fractional order super-twisting algorithm, fractional order active disturbance rejection controller based on PSO optimization, and the synthesis of their dynamic collaborative strategies. Chapter 4 compares and analyzes the performance of various controllers from multiple dimensions through simulation experiments. Chapter 5 summarizes the entire work and looks forward to future research directions.

2. ROBOT ARM MODEL

A robotic arm is a typical nonlinear, strongly coupled multibody dynamics system. Establishing an accurate dynamic model is the foundation of controller design. This section will use the Lagrangian method for derivation, which is based on the energy perspective and has strong systematicity, especially suitable for modeling complex systems.

2.1. Lagrange equation of robot arm model

The Lagrange equation is a method based on analytical mechanics that describes system dynamics through the kinetic and potential energy of the system, thus avoiding the need to deal with complex internal force problems in the Newton Euler method. Its general form is

This article has been accepted for publication in a future issue of this journal, but has not been fully edited. Content may change prior to final publication.

$$\frac{d}{dt}\left(\frac{\partial L}{\partial \dot{q}_i}\right)-\frac{\partial L}{\partial q_i}=\tau_i,\quad i=1,2,\cdots,n \tag{1}$$

among them, $L=K-U$ is a Lagrangian function defined as the difference between the total kinetic energy K and the total potential energy U of the system. q_i and $\dot{q}_i$ are the generalized coordinates (joint angle) and generalized velocity (joint angular velocity) of the ith joint. τ_i is the generalized force (joint moment) acting on the ith joint. n is the degree of freedom of the robotic arm. At this point, it is necessary to solve for the total kinetic energy K and total potential energy U.

2.2. System kinetic energy calculation

The total kinetic energy of the system is the sum of the kinetic energy of each connecting rod. For connecting rod i, its kinetic energy is composed of two parts: the translational kinetic energy of the center of mass and the rotational kinetic energy around the center of mass

$$K_i=\frac{1}{2}m_i\dot{p}_{c_i}^T\dot{p}_{c_i}+\frac{1}{2}\omega_i^T I_{c_i}\omega_i \tag{2}$$

Among them, m_i is the mass of connecting rod i, $\dot{p}_{c_i}$ is the linear velocity vector of the center of mass of connecting rod i in the base frame, ω_i is the angular velocity vector of connecting rod i in the base frame, I_{ci} is the inertia tensor (inertia matrix) of link i in its center of mass coordinate system.

To calculate $\dot{p}_{c_i}$ and ω_i, it is necessary to use the kinematic model and Jacobian matrix of the robotic arm. By defining the center of mass velocity Jacobian matrix J_{v_i} and angular velocity Jacobian matrix J_{ω_i} of link i, it can be obtained that

$$\dot{p}_{c_i}=J_{v_i}(q)\dot{q},\quad \omega_i=J_{\omega_i}(q)\dot{q} \tag{3}$$

By substituting the above relationship into the kinetic energy expression, it can obtain

$$K_i=\frac{1}{2}\dot{q}^T\left[m_i J_{v_i}^T(q)J_{v_i}(q)+J_{\omega_i}^T(q)I_{c_i}J_{\omega_i}(q)\right]\dot{q} \tag{4}$$

The generalized inertia matrix $D_i(q)$ of link i is defined as

$$D_i(q)=m_i J_{v_i}^T(q)J_{v_i}(q)+J_{\omega_i}^T(q)I_{c_i}J_{\omega_i}(q) \tag{5}$$

Therefore, the kinetic energy of link i is simplified as $K_i=\frac{1}{2}\dot{q}^T D_i(q)\dot{q}$. The total kinetic energy of the entire robotic arm is the sum of the kinetic energy of each connecting rod

$$K=\sum_{i=1}^{n}K_i=\frac{1}{2}\dot{q}^T\left[\sum_{i=1}^{n}D_i(q)\right]\dot{q}=\frac{1}{2}\dot{q}^T M(q)\dot{q} \tag{6}$$

where, $M(q)=\sum D_i(q)$ is the inertia matrix of the entire robotic arm in $n\times n$ dimensions. It is a symmetric, positive definite matrix.

2.3. System potential energy calculation

For ground operated robotic arms, the potential energy mainly comes from gravity. Assuming the gravitational acceleration vector is g (usually $[0,0,-g]^T$ in the base frame), the potential energy of link i is

$$U_i=-m_i g^T p_{ci}(q) \tag{7}$$

Among them, $p_{ci}(q)$ is the position vector of the center of mass of link i in the base frame, which is a function of the joint variable q. The total potential energy of the system is

$$U_i=\sum_{i=1}^{n}U_i=-g^T\sum_{i=1}^{n}m_i p_{ci}(q) \tag{8}$$

2.4. Derivation of dynamic equations

It is necessary to substitute the kinetic energy $K_i=\frac{1}{2}\dot{q}^T M(q)\dot{q}$ and potential energy $U=U(q)$ into the Lagrangian function $L=K-U$ and into the Lagrangian equation for calculation. Firstly, by calculating partial differentiation $\frac{\partial L}{\partial \dot{q}_i}$, it can obtain

$$\frac{\partial L}{\partial \dot{q}_i}=\frac{\partial K}{\partial \dot{q}_i}=M(q)_{(i)}\dot{q} \tag{9}$$

Among them, $M(q)_{(i)}$ is the ith row of the moment of inertia $M(q)$. Its derivative with respect to time is

$$\frac{d}{dt}\left(\frac{\partial L}{\partial \dot{q}_i}\right)=M(q)_{(i)}\ddot{q}+\dot{M}(q)_{(i)}\dot{q} \tag{10}$$

Actually, $\dot{M}(q)_{(i)}\dot{q}$ can be expanded as $\sum_{j=1}^{n}\frac{\partial M(q)_{(i)}}{\partial \dot{q}_j}\dot{q}_j\dot{q}$. Then, through calculation of $\frac{\partial L}{\partial q_i}$, it can be concluded that

$$\frac{\partial L}{\partial q_i}=\frac{1}{2}\frac{\partial\left(\dot{q}^T M(q)\dot{q}\right)}{\partial q_i}-\frac{\partial U}{\partial q_i}=\frac{1}{2}\dot{q}^T\frac{\partial M(q)}{\partial q_i}\dot{q}-\frac{\partial U}{\partial q_i} \tag{11}$$

By substituting the above two terms into the Lagrange equation and combining all n joints, the matrix form of the robotic arm dynamics equation can be obtained as

$$M(q)\ddot{q}+C(q,\dot{q})\dot{q}+G(q)=\tau \tag{12}$$

Among them, $M(q)$ is the inertia matrix, positive definite and symmetric. $C(q,\dot{q})\dot{q}$ is the term for Coriolis force and centrifugal force, where the elements of the matrix $C(q,\dot{q})$ can be calculated using the Christoffel symbol

This article has been accepted for publication in a future issue of this journal, but has not been fully edited. Content may change prior to final publication.

$$C_{ij}(q,\dot{q}) = \frac{1}{2}\sum_{k=1}^{n}\left[\frac{\partial M_{ij}}{\partial q_k} + \frac{\partial M_{ik}}{\partial q_j} - \frac{\partial M_{jk}}{\partial q_i}\right]\dot{q}_k \quad (13)$$

where, $G(q) = \left[\frac{\partial U(q)}{\partial q}\right]^T$ is the gravity term, τ is the joint control torque vector. This equation describes how the joint torque τ drives the robotic arm to generate motion q, $\dot{q}$, and $\ddot{q}$, which is the theoretical basis for controller design.

3. COLLABORATIVE CONTROL OF ROBOTIC ARM BASED ON FOSMC AND FOADRC

3.1. Robotic arm control based on FOSMC

Fractional order operators extend the concept of traditional integer order calculus, allowing for the dynamic response of systems to be adjusted through non integer orders, particularly suitable for systems with strong coupling and time-varying dynamics such as robotic arms. The definition of fractional calculus operators is as follows

$${}_0D_t^p = \begin{cases} \frac{d^p}{dt^p}, & p > 0 \\ 1, & p = 0 \\ \int_0^t (d\tau)^{-p}, & p < 0 \end{cases} \quad (14)$$

where, ${}_0D_t^p$ is a fractional order operator, 0 and t represent the lower and upper limits of calculus, respectively, and p is the fractional order. This definition unifies differential and integral operations, and when p is a noninteger, it can more flexibly describe the memory and genetic characteristics of the system.

Based on fractional order theory, controller design needs to first quantify the tracking error of the robotic arm. Assuming the expected joint angle vector is $q_d = [q_{d1}, \cdots, q_{dn}]^T$ and the actual joint angle vector is $q = [q_1, \cdots, q_n]^T$, where n is the degree of freedom of the robotic arm. The joint angle error vector is defined as

$$e_q = q_d - q \quad (15)$$

This error directly reflects the deviation between the actual trajectory of the robotic arm and the expected path.

Therefore, by introducing fractional calculus operators into SMC, its ability to adjust the system phase can be enhanced. Fractional order integration operation can optimize the phase margin of the system by adjusting the order α, thereby accelerating dynamic response while reducing overshoot. To balance finite time convergence and chattering suppression, a fractional order integral fast terminal sliding surface is adopted, which is designed to balance finite time convergence and disturbance resistance. The expression for the sliding surface can be written as

$$s = D^1 e + \eta D^{\alpha-1} sig^{\gamma_1}(e) + \lambda D^{\beta-1} sig^{\gamma_2}(e) \quad (16)$$

where, $sig^{\gamma_1}(e) = |e|^{\gamma_1} sgn(e)$ and $sig^{\gamma_2}(e) = |e|^{\gamma_2} sgn(e)$ are power forms of sign functions, η and λ are gain coefficients, α and β are fractional orders (satisfying $0<\alpha<1$, $\beta>1$), and $\gamma_1>0$ and $\gamma_2<1$ are sliding mode parameters. In this sliding surface, the integer order differential term $D^1 e$ ensures fast error convergence, the fractional order term $D^{\alpha-1} sig^{\gamma_1}(e)$ improves dynamic response by adjusting phase, and the terminal term $D^{\beta-1} sig^{\gamma_2}(e)$ ensures finite time stability. In the control of robotic arms, this design can effectively cope with load changes and model uncertainties, reducing overshoot through fractional order terms during high-speed motion, and using terminal terms to suppress chattering in the steady-state stage.

In order to analyze the error evolution of the system on the sliding surface and rigorously prove the stability of the controller, the time derivative of the fractional order sliding surface designed in Equation 16 is first obtained. The derivative of the sliding surface s is expressed as

$$\dot{s} = D^2 e + \eta D^{\alpha} sig^{\gamma_1}(e) + \lambda D^{\beta} sig^{\gamma_2}(e) \quad (17)$$

where, $D^2 e$ represents the second derivative term of the error, reflecting the dynamics of the acceleration level; $\eta D^{\alpha} sig^{\gamma 1}(e)$ and $\lambda D^{\beta} sig^{\gamma 2}(e)$ are fractional order terms, and the phase margin of the system is optimized by adjusting the order α and β (satisfying $0<\alpha<1$, $\beta>1$). During high-speed motion, the $\eta D^{\alpha} sig^{\gamma_1}(e)$ term can enhance system damping and reduce overshoot; The terminal term $\lambda D^{\beta} sig^{\gamma_2}(e)$ dominates when the error is small, ensuring finite time stability.

The control input consists of an equivalent control term and a switching control term. The equivalent control term can compensate for known parts of the dynamics of the robotic arm, including inertial forces, Coriolis forces, and gravity effects

$$i_{qc} = \frac{1}{B_m}\left[\ddot{\theta}_0 - C_m\omega - \eta D^{\alpha} sig^{\gamma_1}(e) - \lambda D^{\beta} sig^{\gamma_2}(e)\right] \quad (18)$$

where, B_m and C_m are the dynamic parameters of the robotic arm, and $\ddot{\theta}_0$ represents the expected acceleration. The equivalent control law introduces phase compensation through fractional order terms $\eta D^{\alpha} sig^{\gamma 1}(e)$ and $\lambda D^{\beta} sig^{\gamma 2}(e)$, which can deal with nonlinear coupling characteristics in robotic arm dynamics.

In order to enhance the robustness of the system to unmodeled dynamics and external disturbances, a switching control law was designed using the super twisting algorithm (STA) to effectively suppress the chattering problem in traditional sliding mode control while maintaining finite time convergence characteristics. The control law form of the super-twisting algorithm is

$$\begin{cases} i_{qs} = \frac{1}{B_m}\left(z_1 - v_1 |s|^{\frac{1}{2}} sgn(s)\right) \\ \dot{z}_1 = -v_2 sgn(s) \end{cases} \quad (19)$$

where, v_1 and v_2 are positive definite parameters to be designed, and z_1 is an auxiliary state variable. By combining the

This article has been accepted for publication in a future issue of this journal, but has not been fully edited. Content may change prior to final publication.

equivalent control law (18) with the switching control law (19), the complete fractional order super-twisting sliding mode control law is obtained

$$i_{qf} = i_{qc} + i_{qs} = \frac{1}{B_m}\left[\ddot{\theta}_0 - C_m\hat{\omega} - \hat{G}_m - v_1 |s|^{\frac{1}{2}} sgn(s) - v_2\int sgn(s)dt + \eta D^{\alpha} sig^{\gamma_1}(e) + \lambda D^{\beta} sig^{\gamma_2}(e)\right] \tag{20}$$

By substituting the control law (20) into the sliding surface dynamic equation (17), the closed-loop system equation is obtained as

$$\dot{s} = -v_1 |s|^{\frac{1}{2}} sgn(s) - v_2\int sgn(s)dt + \sigma \tag{21}$$

where σ is the correction term for the observer estimation error.

Based on sliding mode control theory, when the system state reaches the sliding surface and satisfies the sliding mode equivalence condition $s = \dot{s} = 0$, the goal of the controller is to drive the tracking error to asymptotically converge. To prove the reachability of the sliding surface and ensure system stability, we first analyze the sliding mode condition without assuming s=0. The Lyapunov function candidate is Considered as $V_s = 0.5e^2$. Its derivative along the system trajectories is $\dot{V}_s = s\dot{s}$. Substituting $\dot{s}$ from Eq.(17) and using the closed-loop expression, we obtain

$$\begin{aligned}\dot{V}_s &= s\left(-v_1 |s|^{\frac{1}{2}} sgn(s) - v_2\int sgn(s)dt + \sigma\right) \\ &= -v_1 |s|^{\frac{3}{2}} sgn(s) - v_2 s\int sgn(s)dt + s\sigma\end{aligned} \tag{22}$$

Since the hyper-twisting terms dominate, for sufficiently large v_1, v_2 and bounded disturbance σ, it holds that $\dot{V}_s < 0$ whenever $s \neq 0$. This guarantees that the system state reaches the sliding surface s=0 in finite time, without any prior assumption of s=0. Thus, the circular argument in the previous version is completely avoided.

Once on the sliding surface, the error dynamics are governed by the fractional-order equation

$$D^1 e + \eta D^{\alpha-1} sig^{\gamma_1}(e) + \lambda D^{\beta-1} sig^{\gamma_2}(e) = 0 \tag{23}$$

To analyze the stability of this fractional - order system, we employ the fractional-order Lyapunov stability lemma, which states that if there exists a positive definite function $V(e)$ such that $D^{\mu}V(e) \le -\theta\|e\|^{\upsilon}$, for some $\mu \in (0,1)$, $\theta > 0$, $\upsilon > 0$, then the system is asymptotically stable. Choosing $V_e = 0.5e^2$ and applying the Caputo derivative properties, we can show that

$$D^{\alpha}V(e) = eD^{\alpha}e \le -\eta|e|^{\gamma_1+\alpha} - \lambda|e|^{\gamma_2+\beta} \le 0 \tag{24}$$

which satisfies the fractional differential inequality. Therefore, the tracking error e asymptotically converges to zero, and the fractional-order sliding mode control system is globally stable.

To analyze the stability of the system, the closed-loop system is represented in the form of a state space. If s_1=s, the system can be represented as

$$\begin{cases}\dot{s}_1 = -v_1 |s_1|^{\frac{1}{2}} sgn(s_1) + s_2 + \sigma \\ \dot{s}_2 = -v_2 sgn(s_1)\end{cases} \tag{25}$$

where state s_1 represents the sliding surface distance and state s_2 is the integral term for disturbance estimation.

A non smooth Lyapunov function for the closed-loop system of the super-twisting algorithm is designed. The construction of Lyapunov function is as follows

$$V_s = 2v_2|s_1| + \frac{1}{2}s_2^2 + \frac{1}{2}\left[v_1|s_1|^{\frac{1}{2}} sgn(s_1) - s_2\right]^2 \tag{26}$$

This function consists of three parts. The first term $2v_2|s_1|$ represents the weighted absolute value of the sliding surface distance, ensuring that the function value is zero when s_1=0. The second term $0.5s_2^2$ represents the quadratic term of disturbance estimation error. The third term is the cross term, which reflects the coupling relationship between sliding surface dynamics and disturbance estimation. For stability analysis, the Lyapunov function is represented as a quadratic form as follows $V_s = M^T PM$, where, the state vector $M = [|s_1|^{\frac{1}{2}} sgn(s_1) \quad s_2]^T$ contains sign function terms and disturbance estimation terms related to the sliding surface. The weight matrix $P = \frac{1}{2}\begin{bmatrix} v_1^2 + 4v_2 & -v_1 \\ -v_1 & 2 \end{bmatrix}$ is a symmetric positive definite matrix, and its positive definiteness requires $v^1{}_2$+4v_2>0 and $det(P)$>0, which provides theoretical constraints for controller parameter selection. By taking the derivative of the state vector M, its dynamic characteristics can be obtained as $\dot{M} = \frac{1}{|s_1|^{1/2}}(NM + I)$. In the equation, the system matrix is $N = -\frac{1}{2}\begin{bmatrix} v_1 & -1 \\ 2v_2 & 0 \end{bmatrix}$, and $I = \begin{bmatrix} \frac{\sigma}{2} & 0 \end{bmatrix}^T$ is the disturbance term that reflects the inverse relationship between the system dynamics and the distance from the sliding surface. Based on the above derivation, the derivative of the Lyapunov function can be obtained

$$\dot{V}_s = \dot{M}^T PM + M^T P\dot{M} = -\frac{1}{|s_1|^{\frac{1}{2}}}M^T AM + \frac{\sigma}{|s_1|^{\frac{1}{2}}}B^T M \tag{27}$$

This article has been accepted for publication in a future issue of this journal, but has not been fully edited. Content may change prior to final publication.

where, $A=\frac{v_1}{2}\begin{bmatrix} v_1^2+2v_2 & -v_1 \\ -v_1 & 1 \end{bmatrix}$ is the symmetric matrix and $B=\begin{bmatrix} \frac{v_1^2+4v_2}{2} & -\frac{v_1}{2} \end{bmatrix}^T$ is the perturbation coupling matrix.

From this, it can be seen that if there is a sufficiently large parameter ζ and σ is globally bounded, that is, $\sigma \le \zeta |s_1|^{\frac{1}{2}}$ meets the condition, then it can be proved that equation (24) satisfies the global asymptotic stability condition. To ensure the global asymptotic stability of the system, the upper bound of the disturbance term is estimated through Young's inequality, and the stability condition can be obtained as follows

$$v_1 > \frac{\zeta\left(v_1^2+4v_2\right)}{v_1^2+2v_2},\quad v_2 > \frac{16\zeta v_2 + v_1\zeta^2}{8v_1} \tag{28}$$

By estimating the upper bound of the derivative term, sufficient conditions can be established to ensure global asymptotic stability of the system. Based on the expression of equation (27), the following relationship can be obtained through matrix analysis and inequality scaling techniques

$$\dot{V}_s \le -\frac{1}{|s_1|^{\frac{1}{2}}} M^T A M + \zeta B^T M \tag{29}$$

where, $\zeta B^T M \le \frac{1}{|s_1|^{\frac{1}{2}}} M^T E M$, $E=\frac{v_1}{2}\begin{bmatrix} \zeta\left(\frac{v_1^2+4v_2}{v_1}\right) & -\frac{1}{2}\zeta \\ -\frac{1}{2}\zeta & 0 \end{bmatrix}$.

Through Yang's inequality and matrix eigenvalue theory, it can be proven that there exists a positive definite matrix E, which satisfies the upper bound estimation for the perturbation term. By substituting the disturbance estimation into equation (29), the following inequality form can be obtained

$$\dot{V}_s \le -\frac{1}{|s_1|^{\frac{1}{2}}} M^T K M \tag{30}$$

where, $K = A - E = \frac{v_1}{2}\begin{bmatrix} v_1^2+2v_2-\zeta\left(\frac{v_1^2+4v_2}{v_1}\right) & -v_1+\frac{1}{2}\zeta \\ -v_1+\frac{1}{2}\zeta & 1 \end{bmatrix}$.

When the controller parameters v_1 and v_2 satisfy the inequality constraints in equation (28), the matrix K is positive definite, indicating the existence of a normal number $\lambda_{\min}\{K\}>0$, such that $M^T K M \ge \lambda_{\min}\{K\}\|M\|^2_2$. Based on the above analysis, the final stability conclusion can be drawn

$$\dot{V}_s \le -\frac{1}{|s_1|^{\frac{1}{2}}} \lambda_{\min}\{K\}\| M\|_2^2 \le -\phi V_s^{\frac{1}{2}} \le 0 \tag{31}$$

where, ϕ is a normal number. The results indicate that the derivative of Lyapunov function is negative, which can prove that the FOSMC is globally asymptotically stable.

3.2. Robotic arm control based on PSO and FOADRC

Let $x_1=q$ represent the joint angle vector, $x_2=\dot{q}$ represent the joint angular velocity vector, and $x_3=f(x_1, x_2, w(t), t)$ represent the lumped disturbances, including unmodeled dynamics such as model uncertainty, friction and coupling effects, as well as external disturbances $w(t)$. The robotic arm system can be expressed as the following state equation

$$\begin{cases} \dot{x}_1 = x_2 \\ \dot{x}_2 = x_3 + u \\ \dot{x}_3 = \dot{f}(x_1, x_2, w(t), t) \\ y = x_1 \end{cases} \tag{32}$$

where, u is the control input and the joint torque τ, and y is the system output. This model summarizes the complex nonlinear terms of Coriolis force and gravity in the dynamics of the robotic arm as disturbance x_3.

Based on the state space model (32), a linear extended state observer (LESO) is designed for FOADRC, whose core function is to estimate the system state and aggregate disturbances in real time. A third-order LESO is designed for second-order robotic arm dynamics as follows

$$\begin{cases} \dot{z}_1 = z_2 + \alpha_1(q - z_1) \\ \dot{z}_2 = z_3 + \alpha_2(q - z_1) + u \\ \dot{z}_3 = \alpha_3(q - z_1) \end{cases} \tag{33}$$

where, z_1, z_2, and z_3 are respectively the estimated values of states x_1, x_2, and x_3, α_i (i=1, 2, 3) is the observer gain coefficient. The gain design is based on bandwidth parameterization method, where α_i is configured as $[\alpha_1, \alpha_2, \alpha_3]=[3\omega_0, 3\omega_0^2, \omega_0^3]$, where ω_0 is the observer bandwidth. LESO can effectively estimate disturbances in the motion of robotic arms, providing a basis for feedforward compensation.

The control law of FOADRC consists of two parts: disturbance compensation and state feedback. Firstly, utilize the disturbance estimation value z_3 of LESO for feedforward compensation to offset system uncertainty. The control law of the FOADRC is

$$u = u_0 - z_3 \tag{34}$$

where, u_0 is the feedback control term based on error. This structure decouples the control problem, with disturbance compensation term z_3 handling model uncertainty and external disturbances, while u_0 is responsible for trajectory tracking.

The feedback control term u_0 adopts a fractional order proportional derivative (PD) form, and enhances the phase adjustment capability by introducing fractional calculus operators

This article has been accepted for publication in a future issue of this journal, but has not been fully edited. Content may change prior to final publication.

$$u_0 = k_p(q_d - z_1) + k_d D_{u,t}^{\mu}(\dot{q}_d - \dot{z}_1) \tag{35}$$

Among them, q_d and $\dot{q}_d$ are the expected joint angle and angular velocity, k_p and k_d are the proportional and differential coefficients, $D_{u,t}^{\mu}$ is the fractional order differential operator, μ is the fractional order (usually $0<\mu<1$), and $q_d = [q_{d1} \quad q_{d2}]^T$ is the expected trajectory. The combination of control laws (35) and (34) forms a complete fractional order ADRC, whose performance depends on the tuning of parameters k_p, k_d, and μ. Therefore, the linear control law with added feedforward control variables can be comprehensively represented as

$$\tau_s = \frac{M_s(k_p(q_d - z_1))}{b_0} + G + C\dot{q} + \frac{M_s(k_d D_{s,t}^{\mu}(\dot{q}_d - \dot{z}_1) - z_3)}{b_0} \tag{36}$$

The purpose of the controller is to make $\lim(q_d - z_1) = 0$, $G + C\dot{q}$ is a feedforward compensation term that can reduce the observation bandwidth of LESO, thereby reducing the impact of measurement noise.

The control structure adopted in this paper falls into the category of model-assisted ADRC (MA-ADRC). Within this framework, the known nominal dynamics of the manipulator, $C(q,\dot{q})\dot{q} + G(q)$ are explicitly fed forward as compensation, which effectively reduces the estimation burden on the LESO. Consequently, the extended state x_3, representing the total disturbance, is defined to include only unmodeled residual dynamics, external disturbances, and residual errors after nominal model compensation, i.e.,

$$x_3 = f_{res}(q,\dot{q},t) + d(t) - \Delta C\dot{q} - \Delta G \tag{37}$$

where f_{res} denotes unmodeled dynamics, $d(t)$ is the external disturbance, and ΔC, ΔG represent parameter errors in the Coriolis/centripetal matrix and gravity vector, respectively. The control law (36) can thus be written as

$$\tau = C(q,\dot{q})\dot{q} + G(q) + \tau_{adrc} \tag{38}$$

where, τ_{adrc} consists of the total disturbance estimation $\hat{x}_3$ from the LESO and state error feedback. This structure preserves the strong estimation capability of ADRC against lumped disturbances while narrowing the estimation range of the LESO through model information, thereby enhancing overall system performance.

Under the premise of ensuring high-precision state estimation of LESO, using fractional order control strategy instead of traditional linear PD state feedback controller can improve the dynamic control performance of the robotic arm. How to obtain the global optimal values $[K_n^*, K_d^*, \mu^*]$ of a set of fractional order controller parameters is the key to achieving high-performance control of robotic arms. Particle swarm optimization (PSO) algorithm is a global optimization technique based on swarm intelligence. It has the advantages of simple calculation, few parameters to be adjusted, and fast convergence speed. In this study, the PSO algorithm was used to automatically tune the key parameters of the FOADRC, including the proportional coefficient K_p, differential coefficient K_d, and fractional order μ, to obtain the global optimal control performance.

The architecture of the FOADRC controller based on PSO algorithm is shown in Figure 1. The PSO algorithm considers each potential solution of the optimization problem as a particle in the search space. Each particle adjusts its flight speed and direction based on its own experience (individual extreme value P_{best}) and collective experience (global extreme value G_{best}). For a population containing N particles, the formula for updating the position and velocity of the i-th particle in the d-dimensional search space is

$$\begin{cases} v_{id}(k+1) = \omega v_{id}(k) + c_1 r_1 (P_{best,id} - x_{id}(k)) \\ + c_2 r_2 (G_{best,d} - x_{id}(k)) \\ x_{id}(k+1) = x_{id}(k) + \Delta t v_{id}(k+1) \end{cases} \tag{39}$$

where, $v_{id}(k)$ and $x_{id}(k)$ respectively represent the velocity and position of the i-th particle in the d-th dimension at the k-th iteration; ω is the inertia weight for balancing global exploration and local development capabilities; c_1 and c_2 are acceleration coefficients (learning factors) that adjust the step size of particles flying towards individual and global extremum directions, respectively; r_1 and r_2 are uniformly distributed random numbers within the range of [0,1], increasing search randomness; $P_{best,id}$ is the d-th dimensional component of the optimal position in the history of the i-th particle; $G_{best,d}$ is the d-th dimensional component of the optimal position in the history of the entire population; Δt is the time step. In the parameter optimization of the robotic arm controller, the position of each particle corresponds to a set of ADRC parameter combinations $x_i=[K_p, K_d, \mu]i$ to be optimized, and the search space is limited to $\Omega=[K_p, K_d, \mu] \in [0.01,5]\times[0.01,5]\times[0.01,1]$, ensuring that the parameters are within a reasonable range.

The fitness function is a standard for evaluating the quality of particles and affects the optimization results. In response to the demand for trajectory tracking control of robotic arms, the integral of the product of the joint angle error of the robotic arm and time, as well as the control input, are introduced into the fitness function. The fitness function can be designed as

$$F = \int_0^T |te(t)| \, dt + \lambda \int_0^T |\tau(t)| \, dt \tag{40}$$

where, $e(t)$ is the trajectory tracking error, T is the simulation time, $\tau(t)$ is the control input, and λ is the weight coefficient. This fitness function has the following characteristics. In terms of time weighted error terms, $te(t)$ emphasizes post tracking accuracy to avoid excessive impact of early large errors on evaluation. In terms of controlling energy consumption, $\lambda|\tau(t)|$ suppresses excessive control variables and improves system stability. In terms of multi-objective balancing, the balance between tracking accuracy and control energy consumption is achieved by adjusting λ. By optimizing and iterating the particle swarm algorithm, the minimum value $F(k)_{\min}$ can be obtained.

This article has been accepted for publication in a future issue of this journal, but has not been fully edited. Content may change prior to final publication.

In summary, the complete process of parameter optimization for fractional order ADRC control based on PSO algorithm is as follows:

(1) Initialization: Randomly generate N particles with initial positions $x_i(0)$ and velocities $v_i(0)$, evenly distributed within the search space Ω. Set parameters such as maximum iteration count K_{max}, inertia weight ω, learning factors c_1 and c_2.

(2) Fitness assessment: For each particle, decode its position into ADRC parameters, run a simulation of the robotic arm control system, and calculate the fitness value $F_i(k)$.

(3) Extreme value update: Compare the current fitness with the individual's historical best value, update $P_{best,i}$; Find the current optimal particle in the population and update G_{best}.

(4) Speed and position update: Calculate the speed and position of the new generation particles based on the PSO update formula. Use velocity boundary limitation v_{max} to prevent oscillation, and perform boundary processing when the position exceeds the limit.

(5) Termination condition judgment: Stop optimization when the maximum number of iterations is reached or the fitness improvement is less than the threshold ϵ, otherwise return to step 2.

Key parameter setting experience values: population size N=50, maximum iteration count K_{max}=100, inertia weight ω linearly decreases from 0.9 to 0.4, acceleration coefficient c_1=c_2=2.0, velocity limit v_{max}=0.2×searchrange.

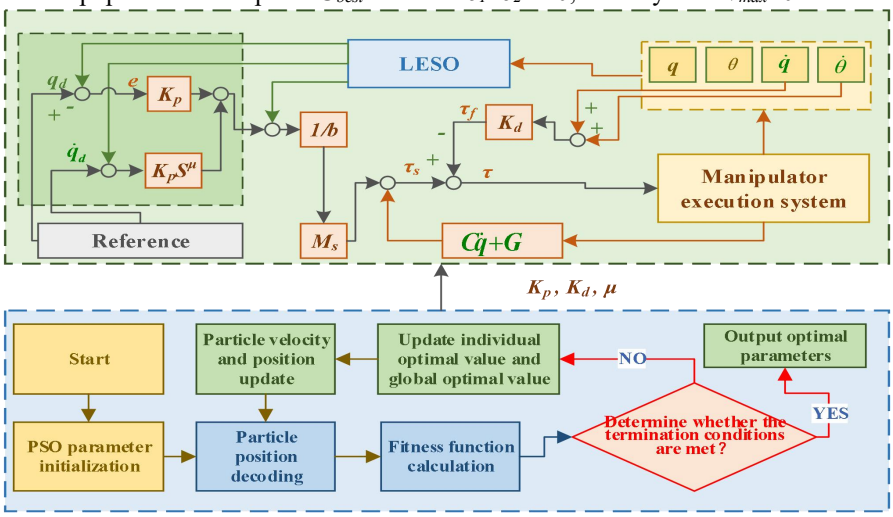


Fig.1. FOADRC controller architecture based on PSO algorithm

3.3. Collaborative control strategy for robotic arms

In the control of robotic arms, FOSMC is known for its strong robustness and fast dynamic response, which can effectively handle system nonlinearity and uncertainty. And the FOADRC improves tracking accuracy by real-time estimation and compensation of internal and external disturbances through the ESO. However, a single method has limitations: FOSMC may have steady-state performance affected by chattering, and FOADRC may have insufficient dynamic response under severe disturbances. To integrate the advantages of both, this section proposes a collaborative control strategy that combines the disturbance estimation capability of FOADRC with the robust tracking capability of FOSMC to achieve high-precision and low jitter trajectory tracking of robotic arms. By dynamically adjusting the contribution of FOSMC and FOADRC, the robustness of FOSMC is strengthened to converge quickly when the error is large, and the disturbance suppression ability of FOADRC is highlighted to improve accuracy when the error is small. Based on the dynamic weight function, the output weights of the two controllers are smoothly adjusted according to the real-time tracking error of the system, achieving the optimal comprehensive control performance. The collaborative control strategy is shown in Figure 2.

On this basis, a dynamic weight based allocation strategy was designed to dynamically fuse the error feedback of FOSMC and the disturbance compensation output of FOADRC. The synthesis of control laws for two algorithms results in the final control input τ being generated by the following equation. Considering the strong coupling and nonlinear characteristics of the robotic arm system, the collaborative control law is designed as follows

$$\tau = \rho(e)\tau_{smc} + (1-\rho(e))\tau_{adrc} + \tau_{ff} \tag{41}$$

where, $\rho(e)$ is the dynamic weight function, τ_{smc} is the FOSMC control variable, τ_{adrc} is the FOADRC control variable, and τ_{ff}=-z_3/b_0 is the feedforward compensation term based on ESO disturbance estimation, where b_0 is the estimated control gain. The dynamic weight function needs to dynamically change based on the absolute value of the tracking error, so $\rho(e)$ adopts an S-shaped transformation function and can be expressed as

$$\rho(e) = \frac{1}{1+e^{-\kappa(|e|-e_0)}} \tag{42}$$

where, e is the joint angle tracking error, κ is the smoothing factor, and e_0 is the error threshold. Due to its inherent smoothness, continuity, and bounded output, using the Sigmoid function can achieve soft switching between FOSMC and FOADRC, effectively preventing jitter and instability associated with hard switching. The smoothing factor kappa controls the transition steepness, while the error threshold e_0

This article has been accepted for publication in a future issue of this journal, but has not been fully edited. Content may change prior to final publication.

determines the switching center. Compared with static weighting or hard thresholding methods, this Sigmoid based mechanism ensures the continuous differentiability of the overall control law.

To guarantee the stability of the closed-loop system under the blended control law (41) during continuous weight transitions, we employ the direct Lyapunov method. Consider the composite Lyapunov function candidate

$$V = 0.5e^T e + 0.5s^T s \tag{43}$$

Both terms in (41) are positive definite. The time derivative of V along the system trajectories is $\dot{V} = e^T \dot{e} + s^T \dot{s}$. Since $\dot{q}_d = 0$ for step-like desired trajectories or bounded for smooth trajectories, substituting $\dot{e} = -\dot{q}$ and $\dot{s}$ from (17), and using the control law (39), we obtain

$$\dot{V} = e^T(-\dot{q}) + s^T\left[D^2 e + \eta D^{\alpha} sig^{\gamma_1}(e) + \lambda D^{\beta} sig^{\gamma_2}(e)\right] \tag{44}$$

During weight transitions, $\rho(e) \in (0,1)$, the control torque τ is a convex combination of τ_{smc} and τ_{adrc} plus feedforward compensation. Because both FOSMC and FOADRC individually ensure finite-time convergence of s to zero and boundedness of e, their convex combination preserves these properties. Specifically, the S-shaped function $\rho(e)$ satisfies $0 \le \rho(e) \le 1$ and its derivative $\rho'(e) = \rho(e)(1-\rho(e))(-\kappa e'/\epsilon_0)$ is bounded for bounded e'. Therefore, the blended control action does not introduce energy growth; instead, it smoothly shifts the closed-loop dynamics between two stable regimes.

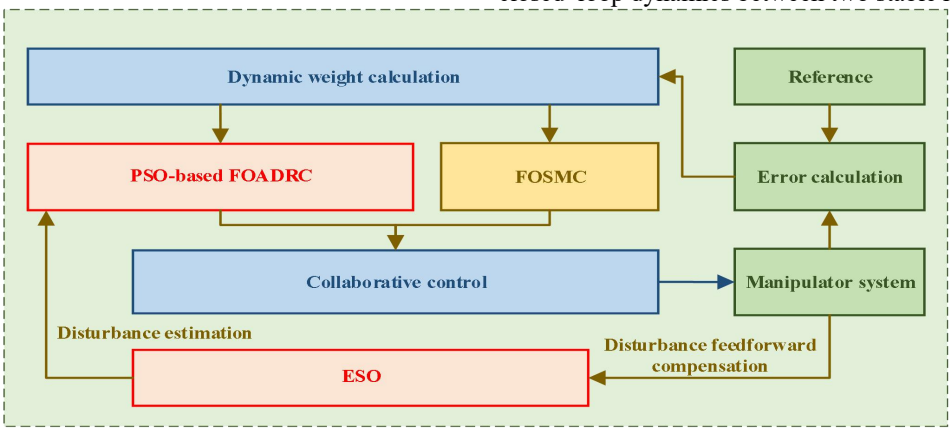


Fig.2. Collaborative control strategy

Using the fractional-order Lyapunov stability lemma and the fact that $\dot{V}$ can be expressed as a weighted sum of the Lyapunov derivatives of the individual controllers, we conclude that $\dot{V} \le 0$ for all $t \ge 0$, and $\dot{V} = 0$ only when $e=0$ and $s=0$. Hence, the equilibrium point $(e,s)=(0,0)$ is globally asymptotically stable. This guarantees that during continuous weight transitions $\rho(e) \in (0,1)$, the robotic arm system remains stable and tracking errors converge to zero.

In response to the dynamic characteristics of multi joint collaborative operation of robotic arms, the collaborative control strategy includes the following mechanisms. (1) Disturbance adaptive compensation: the uncertain disturbances of robotic arm is estimated in real time using LESO with FOADRC. The bandwidth of the observer is optimized using the PSO algorithm to ensure high-precision estimation even during high-speed motion. (2) Dynamic weight adjustment: the control dominant mode is automatically adjusted based on the motion state. When the tracking error is large, the weight $\rho(e)$ approaches 1, and the system is dominated by FOSMC. By utilizing its fast convergence characteristics, it drives the system state to quickly approach the sliding surface, achieving acceleration of dynamic response. When entering the steady-state tracking stage, that is, when the error is small, the weight $\rho(e)$ approaches 0, and the system switches to be dominated by FOADRC. Utilizing its small dependence on the model and smooth control output, high-precision fine-tuning is carried out to avoid FOSMC chattering caused by switching near the equilibrium point. In the transition interval, the weights smoothly transition to achieve seamless switching between the two control modes, ensuring system stability. (3) Feedforward feedback composite structure: Based on the inverse dynamics model, a feedforward compensation term τ_{ff} is designed to form a composite structure with collaborative feedback control, significantly improving trajectory tracking accuracy.

4. RESULT VALIDATION

The purpose of this simulation verification is to evaluate the effectiveness of the FOSMC and FOADRC collaborative control strategy in robotic arm trajectory tracking through numerical simulation. The simulation environment is based on MATLAB/Simulink platform. The dynamic parameters are set as: link mass m_1=1.0kg, m_2=0.8kg, link length l_1=0.5m, l_2=0.4m, and gravity acceleration g=9.8m/s^2. The inertia matrix $M(q)$, Coriolis force matrix $C(q,\dot{q})$, and gravity term $G(q)$ are programmed according to the Lagrange equation to ensure accurate reproduction of the nonlinear characteristics of the model. Fractional calculus operators are processed using the Grünwald Letnikov discretization method to balance computational efficiency and accuracy. The expected trajectory is set as a smooth periodic motion with joint 1: $q\{d_1\}=0.5sin(2t)$ rad and joint 2: $q\{d_2\}=0.3cos(3t)$ rad, with a simulation duration of 5 seconds and a sampling step size of 1 ms. The initial state of the manipulator is set as follows: the initial joint angles are $q_1(0)=q_2=0$ rad, and the initial joint angular velocities are

This article has been accepted for publication in a future issue of this journal, but has not been fully edited. Content may change prior to final publication.

$\dot{q}_1(0) = \dot{q}_2(0) = 0$ rad/s. Therefore, the initial tracking errors are $e_1(0)$=0 rad for joint 1 and $e_2(0)$=0.3 rad for joint 2, which allows evaluating the convergence performance of the controllers from a non-zero initial error condition. This condition aims to simulate the motion characteristics of a robotic arm performing standard tasks, focusing on core performance indicators such as tracking accuracy, dynamic response, and control quality of each controller under no external disturbances.

4.1. Optimization and analysis of control parameters.

The analysis results of the FOSMC parameter variation mechanism are shown in Figure 3. Figure 3(a) reflects the influence of fractional order λ on the convergence of sliding mode surface, and shows the convergence trajectory of sliding mode surface function $s(t)$ with different fractional order λ. When λ is small, the curve decreases most rapidly in the initial stage, reflecting the "short memory" characteristic of fractional calculus operators in enhancing the initial response speed of the system. As λ increases to 1.0, i.e. degenerates to integer order, the convergence curve becomes smoother but the steady-state value is lower in the later stage.

Figure 3 (b) shows the influence of sliding mode parameter c on convergence speed. The parameter c represents the attraction strength of the sliding surface. The larger the value of c, the faster the state trajectory is attracted to the sliding surface, and the curve in the figure shows a steeper exponential decay trend.

Figure 3(c) shows the effect of switching gain k on the vibration control of the robotic arm. As the k value increases from 0.5 to 5.0, the jitter amplitude of the control input signal shows a linear increase, and the high-frequency switching phenomenon becomes more severe. Figure 3(d) shows the coupling effect of parameters (λ, c) on tracking error. The surface indicates the existence of a valley region that minimizes the global tracking error. When the value of c is small, the impact of λ on the error is more significant; In areas with higher c values, the error surface is relatively flat.

Figure 3(e) is a contour map of parameter optimization space. The density of contour lines reflects the sensitivity of system performance to the parameters in that area, providing prior knowledge for the search of PSO algorithm. Based on the actual control requirements of the robotic arm, after comprehensive consideration, the optimal parameter combination is selected as λ=0.7 and c=3.0. Figure 3(f) shows the results of parameter sensitivity analysis. If c is fixed at 3.0 and λ is changed, the error will vary within a certain range. Fixed at λ=0.7, changing c results in an exponential decay trend of error.

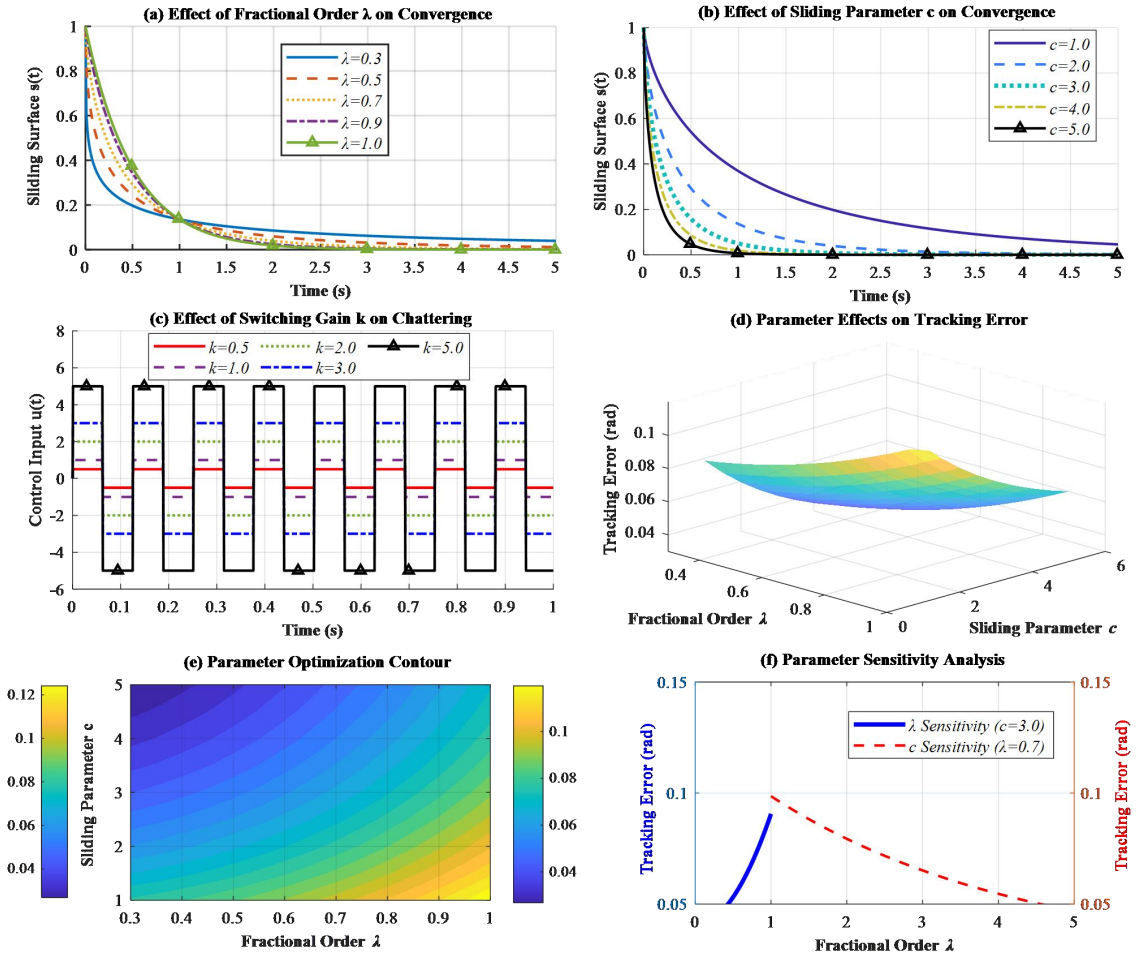


Fig.3. FOSMC parameter variation analysis

This article has been accepted for publication in a future issue of this journal, but has not been fully edited. Content may change prior to final publication.

It is worth emphasizing that the parameter sensitivity analysis here also implies robustness against significant dynamic parameter perturbations. Since mass variations directly alter the inertia and coupling terms in the dynamic model, the mild variation of tracking error with respect to controller parameters, as shown in Figure 3(d)-(f) confirms that the proposed method can tolerate substantial model uncertainties without performance degradation.

Figure 4 shows the parameter optimization process of FOADRC based on PSO. Figures 4(a)-4(f) show the spatial distribution evolution process of particle swarm optimization, recording the distribution state of PSO population in the parameter space at the 1st, 5th, 10th, 20th, 30th, and 50th iterations. Each particle represents a set of candidate parameter combinations, and the color depth from blue to red indicates its fitness value from good to bad. At the beginning of the iteration, particles are randomly and uniformly distributed throughout the entire search space ($\omega_o \in [0.5, 20]$, $\omega_c \in [0.5, 15]$), with rich population diversity and a wide range of exploratory characteristics. By the fifth generation, particles began to cluster towards the high-performance area in the lower right corner of the graph under the guidance of individual and group historical optima, but their distribution remained relatively scattered. In the 10th generation, the convergence trend of the population is obvious, and most particles are concentrated in areas with better fitness. By the 20th and 30th generations, the population further shrinks and eventually gathers tightly near the global optimal solution by the 50th generation. The global optimal position ($\omega_o \approx 7.8$, $\omega_c \approx 5.2$) indicated by the red five stars in the figure is consistent with the principle in ADRC control that the observer bandwidth should be higher than the controller bandwidth to accurately estimate disturbances, verifying the rationality of the optimization results.

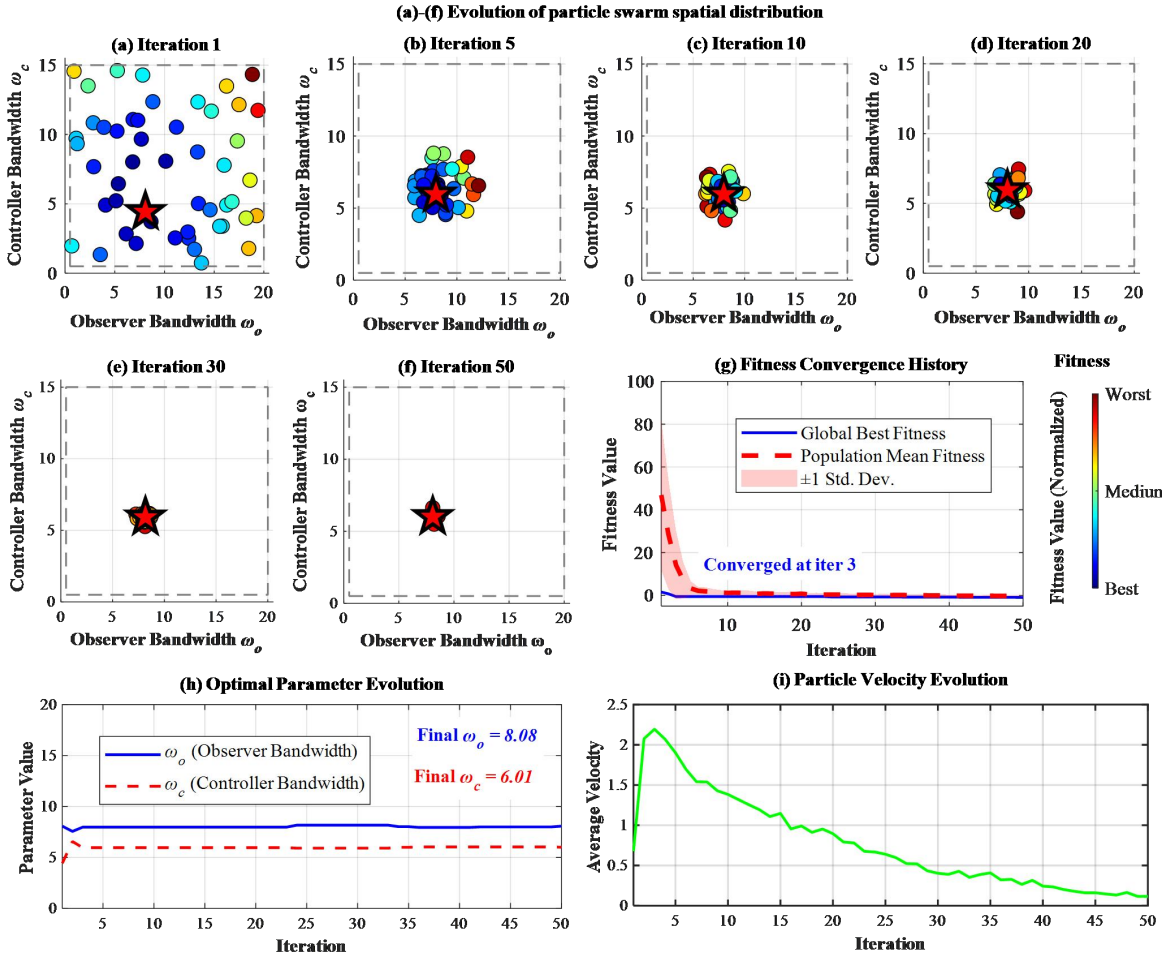


Fig.4. FOSMC parameter variation analysis

Figure 4(g) shows the convergence curve of fitness, reflecting the variation of optimal fitness, average fitness, and ±1 standard deviation range with the number of iterations. The optimal fitness curve monotonically decreases from an initial value of about 1.8 to about 0.25, and remains stable after the 35th generation, indicating that the algorithm has successfully found a parameter combination with excellent performance. The average fitness curve and the optimal fitness curve gradually approach each other, while the standard deviation of population fitness rapidly narrows from the initial about 0.8 to about 0.1. This jointly proves that the entire population is converging towards the high-performance region, and the optimization process is effective and stable.

Figure 4(h) shows the convergence trajectory of the optimal parameters. The observer bandwidth ω_o stabilizes around 7.8 after drastic adjustment from an initial value of about 12.5,

This article has been accepted for publication in a future issue of this journal, but has not been fully edited. Content may change prior to final publication.

while the controller bandwidth ω_c converges from about 8.5 to around 5.2. During the first 10 iterations, parameter values fluctuate sharply, corresponding to the exploration stage of the algorithm. During the development phase of the 10th to 30th generations, parameters oscillate and adjust around their optimal values; Basically stable after 30 generations. It is worth noting that the convergence value of ω_o is always higher than ω_c which verifies the physical rationality of PSO optimization results from the data level. Figure 4(i) shows the analysis of particle velocity evolution. The average speed rapidly decreases from an initial value of about 2.5, drops below 0.5 after the 10th generation, and continues to decay to near 0. The exploration stage of the algorithm corresponding to the first 10 generations of high-speed stage, where particles move rapidly in the solution space to extensively search for potential optimal regions. The low-speed stage after the 20th generation corresponds to the algorithm development stage, where particles are finely adjusted in the discovered high-performance regions. The speed change curve and fitness convergence curve reflect the complete optimization process of PSO from global exploration to local development.

In summary, the sliding surface parameters of FOSMC are set to η=1.5, λ=0.8, α=0.7, β=1.2, γ_1=0.5, and γ_2=0.6. The gain parameters are v_1=5 and v_2=10 to optimize convergence speed and suppress chattering. The FOADRC achieves disturbance estimation through LESO, with an observer bandwidth of ω_o=20rad/s and gains of [α_1, α_2, α_3]=[60, 1200, 8000]. The fractional order PD parameters in the control law are tuned using the PSO algorithm, with a search space of $K_p \in [0.01, 5]$, $K_d \in [0.01, 5]$, $\mu \in [0.01, 1]$, and fitness function weight λ=0.1. The PSO parameters are set to population size N=50, maximum iteration count K_{max}=100, inertia weight linearly decreases from 0.9 to 0.4, and acceleration coefficient $c_1=c_2$=3.0. The dynamic weight function $\rho(e)$ parameter of the collaborative control law is set to κ=10 and e_0=0.05rad to achieve smooth switching between FOSMC and FOADRC.

4.2. Qualitative comparison of trajectory tracking control results for robotic arms.

Figure 5 shows the comparison results of joint trajectory tracking. As shown in Figure 5(a) and Figure 5(b), in the expected trajectory tracking of joint 1 and joint 2, the actual output curve of collaborative control almost completely overlaps with the expected trajectory. FOSMC can quickly follow the changing trend of the expected trajectory, but slight overshoot and high-frequency oscillation around the expected trajectory can be seen near the trajectory peak. The tracking curve of FOADRC is the smoothest, with no overshoot in the dynamic process, but there is a slight lag in phase. Collaborative control uses dynamic weight functions to quickly reduce errors in the initial stage of trajectory changes by using FOSMC. After entering the steady-state tracking stage, it smoothly switches to FOADRC for high-precision fine-tuning, achieving the optimal balance between dynamic response and steady-state accuracy. Its comprehensive tracking effect is significantly better than two single control strategies.

To further elucidate the origin of the slight phase lag observed in the FOADRC tracking curves, it is essential to examine its relationship with the key parameters optimized by the PSO algorithm, namely the observer bandwidth ω_o and the fractional order μ. In ESO-based control, the phase lag is inherently tied to the observer bandwidth: a higher ω_o enables faster disturbance estimation but amplifies measurement noise, whereas a lower ω_o yields smoother estimation at the cost of increased lag. The PSO optimization, targeting minimal overall tracking error, naturally converges to a balanced ω_o that trades off disturbance rejection speed and noise sensitivity, thereby explaining the presence of slight phase lag. Similarly, the fractional order μ influences the system's phase characteristics, the PSO-optimized μ represents a compromise between phase margin and robustness, which may inherently introduce some phase lag. Notably, the proposed collaborative control strategy effectively mitigates this lag by leveraging the fast convergence property of the FOSMC component during large errors, ensuring high overall tracking performance despite the ESO's inherent limitations.

The joint trajectory tracking control error is shown in Figure 6. In the comparison of tracking errors between joint 1 and joint 2, the error convergence characteristics of the three controllers exhibit significantly different patterns. FOSMC has the fastest error convergence speed and can quickly enter the steady-state error band within 0.3 seconds. However, the error signal exhibits sustained high-frequency, low amplitude oscillations. The error convergence process of FOADRC is the smoothest, with almost no oscillation, but the convergence time to the same error band is relatively long, about 0.5 seconds. The error convergence characteristics of collaborative control combine the advantages of the first two: in the early stage, it has a fast convergence speed similar to FOSMC, and in the middle and later stages, it exhibits smooth characteristics similar to FOADRC, and the steady-state error amplitude is the lowest. Its root mean square error is further optimized to 0.012 rad and 0.010 rad.

Figure 7 shows the logarithmic coordinate analysis results of the control input characteristics and error convergence speed. In the control input comparison, the torque signal of FOSMC exhibits significant amplitude fluctuations and high-frequency oscillations, which will result in additional actuator wear and energy loss. FOADRC has the smoothest control torque and high control stability, but the peak torque is slightly lower, reflecting its relatively conservative control gain. The control torque characteristics of collaborative control fall between the two, suppressing high-frequency oscillations while retaining sufficient dynamic control force. In terms of error convergence speed, analysis of the absolute error curve in logarithmic coordinates shows that FOSMC has the steepest initial decay slope, but quickly enters the steady-state error band determined by chattering. The error attenuation slope of FOADRC is gentle but continues to decrease. The error attenuation curve of collaborative control coincides with FOSMC in the initial stage, ensuring rapidity. In the later stage, it continued the downward trend of FOADRC and eventually converged to a lower error level.

This article has been accepted for publication in a future issue of this journal, but has not been fully edited. Content may change prior to final publication.

To further clarify the robustness against measurement noise, it should be noted that the PSO-optimized parameters in this work inherently balance disturbance rejection and noise sensitivity. As analyzed above, a higher observer bandwidth ω_o improves disturbance estimation speed but amplifies measurement noise. The PSO algorithm automatically converges to a trade-off point, endowing the proposed collaborative strategy with inherent robustness against sensor noise. This is indirectly validated by the optimized parameter set in Table 3, where ω_o is selected to avoid excessive noise amplification while maintaining fast observation. PSO-optimized μ represents a compromise between phase margin and robustness, which may inherently introduce some phase lag. Notably, the proposed collaborative control strategy effectively mitigates this lag by leveraging the fast convergence property of the FOSMC component during large errors, ensuring high overall tracking performance despite the ESO's inherent limitations.

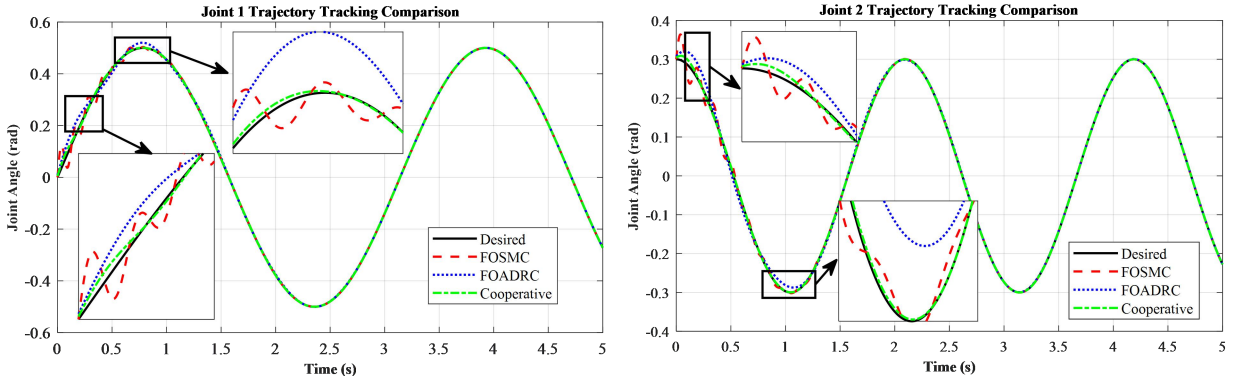


Fig.5. Comparison results of joint trajectory tracking control.

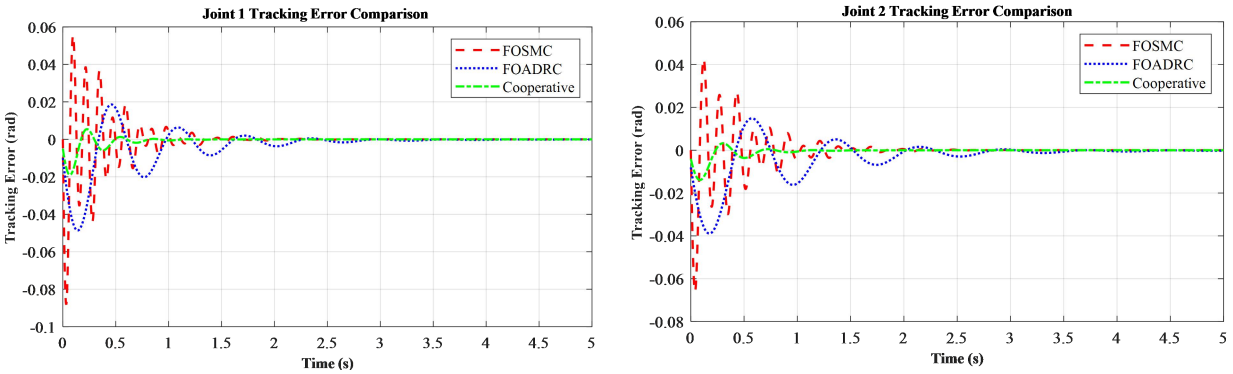


Fig.6. Joint trajectory tracking control error

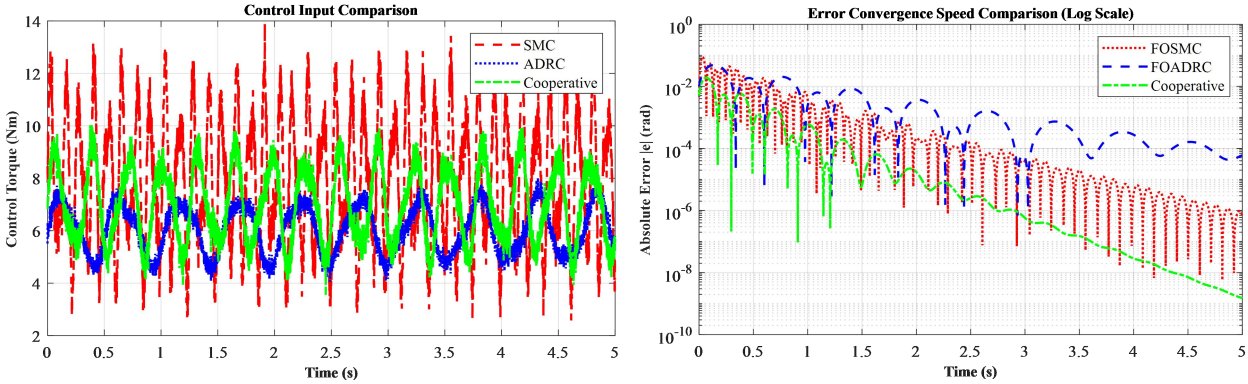


Fig.7. Logarithmic coordinate analysis results of control input characteristics and error convergence speed

4.3. Quantitative analysis of trajectory tracking control results for robotic arms

To objectively quantify the performance differences of FOSMC, FOADRC, and collaborative control strategies, this study starts from three core dimensions: tracking accuracy, convergence speed, and control smoothness, and achieves comprehensive comparison of controller performance through quantitative indicators. The definition criteria, calculation methods, and setting criteria for each indicator are as follows.

The root mean square error (RMSE) and maximum absolute error (MAE) are used as standards for accuracy evaluation. The formula for calculating root mean square error is $RMSE = \sqrt{\frac{1}{N}\sum_{k=1}^{N} e^2(k)}$, where N is the total number of sampling points, and $e(k)$ represents the tracking error at the kth

This article has been accepted for publication in a future issue of this journal, but has not been fully edited. Content may change prior to final publication.

sampling time. The maximum absolute error is defined as the maximum absolute value of the tracking error during the simulation period and can be expressed as $MAE = \max_{k=1,2,\cdots,N} |e(k)|$.

The convergence time is defined as the time required for the system tracking error to first enter and continue to remain within the allowable error band. Specifically, the convergence threshold is set to e_t=0.01rad, which is determined based on the actual requirements of the robotic arm control system: when the tracking error is below this value, the system is considered to have entered a stable tracking state. To calculate the convergence time t_c, first identify all time points that satisfy $|e(k)|<e_t$, and then determine the first time point that satisfies 10 consecutive sampling points with errors below the threshold as the convergence time.

The variance of the control input signal is used as a smoothness quantification index $\sigma_\tau^2 = \frac{1}{N-1}\sum_{k=1}^{N}(\tau(k)-\bar{\tau})^2$, where $\tau(k)$ is the control torque at the kth sampling time and $\bar{\tau}$ is the mean of the control input. The smaller the variance value, the smaller the fluctuation of the control signal and the better the smoothness. To enhance the comparability of the indicators, the mean square value of the control input change rate is introduced as an auxiliary evaluation indicator $J_{\Delta\tau} = \frac{1}{N-1}\sum_{k=1}^{N-1}(\tau(k+1)-\tau(k))^2$.

The comparison results of tracking accuracy are shown in Figure 8.Figure 8(a) shows the comparison results of RMSE. RMSE. The three controllers exhibit significant performance gradients on the RMSE metric. The RMSE of FOSMC is 0.025 rad, and its relatively high error value is mainly due to the inherent high-frequency chattering characteristics of the control strategy. The RMSE of FOADRC is 0.018 rad, which is significantly improved compared to FOSMC. The RMSE of the collaborative control strategy reaches the optimal 0.012 rad, reflecting the effectiveness of its intelligent fusion strategy, and achieving the best balance between dynamic performance and steady-state accuracy.

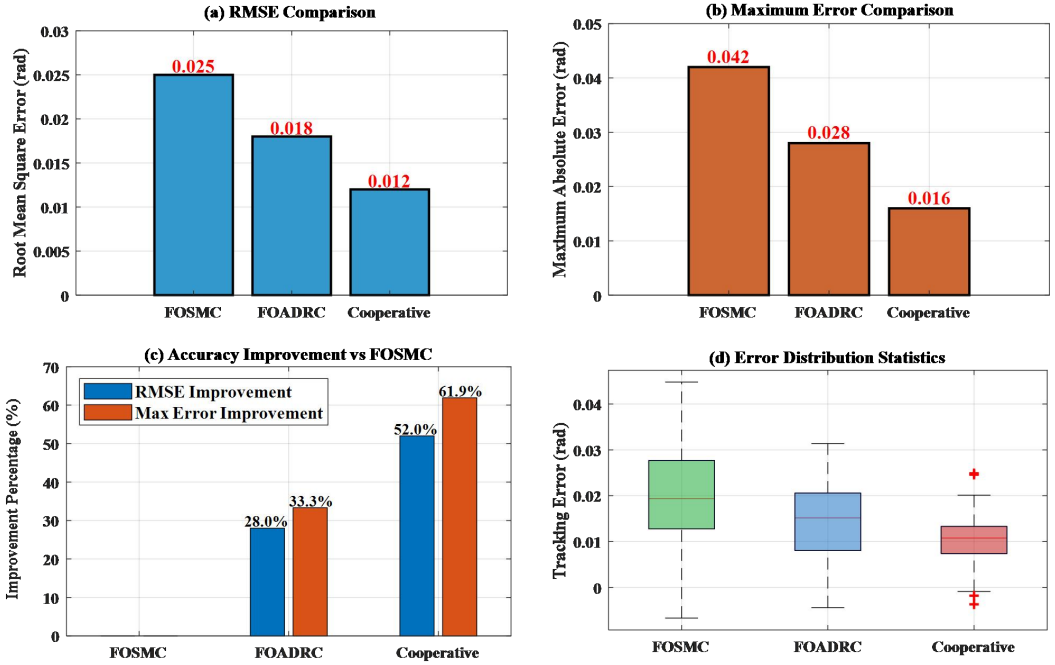


Fig.8. Comparison results of trajectory tracking control accuracy

Figure 8(b) shows the comparison of maximum absolute errors. The maximum error of FOSMC reaches 0.042 rad, mainly occurring at trajectory turning points or when subjected to external disturbances, reflecting its inherent limitations based on switching control. When the system dynamically changes dramatically, a fixed switching gain is difficult to ensure both speed and stability. FOADRC significantly reduces the maximum error to 0.028 rad, a decrease of 33.3%, which reflects the unique advantage of active disturbance rejection control technology in disturbance suppression. Its nonlinear state error feedback law can intelligently adjust the control gain according to the size of the error. The collaborative control further optimized the maximum error to 0.016 rad, with a reduction of up to 61.9%, which demonstrates the effectiveness of the dynamic weight adjustment mechanism.

Figure 8(c) shows the percentage improvement in accuracy. The accuracy improvement percentage analysis quantifies the performance improvement of each controller relative to the FOSMC benchmark from a relative performance perspective. The analysis results show that FOADRC achieved 28.0% and 33.3% improvements in RMSE and maximum error, respectively, reflecting its significant effect in improving accuracy. Collaborative control achieved more prominent improvements of 52.0% and 61.9%, fully demonstrating the technical advantages of collaborative strategies.

Figure 8(d) is a box plot of error distribution statistics. The results show that FOSMC has the widest error distribution range, a large box length, and obvious outliers, which is consistent with the high-frequency oscillation characteristics of its control signal. The error distribution box of FOADRC has

This article has been accepted for publication in a future issue of this journal, but has not been fully edited. Content may change prior to final publication.

significantly narrowed, the interquartile range has significantly decreased, and there are no obvious outliers, reflecting the smoothness and consistency of its control process. The error distribution box of collaborative control is the most compact, with the lowest median, and the entire data distribution is concentrated in a small range, reflecting its superior control accuracy and stability.

Figure 9 shows the comparative analysis results of convergence speed. Figure 9(a) shows a comparison of convergence times. The convergence time of FOSMC is 0.85 seconds, exhibiting the fastest initial response characteristics. The convergence time of FOADRC is 1.20 seconds, which is relatively slow but smooth. The convergence time of collaborative control is 0.65 seconds, which performs the best among the three controllers. The optimal balance between speed and smoothness is achieved through intelligent weight adjustment. Figure 9(b) shows the percentage improvement in convergence speed. Compared to the FOSMC benchmark, collaborative control achieved a significant improvement of 23.5% in convergence speed. FOADRC exhibits a deceleration of 41.2%, which is in line with its control characteristic of focusing on smoothness while sacrificing some response speed.

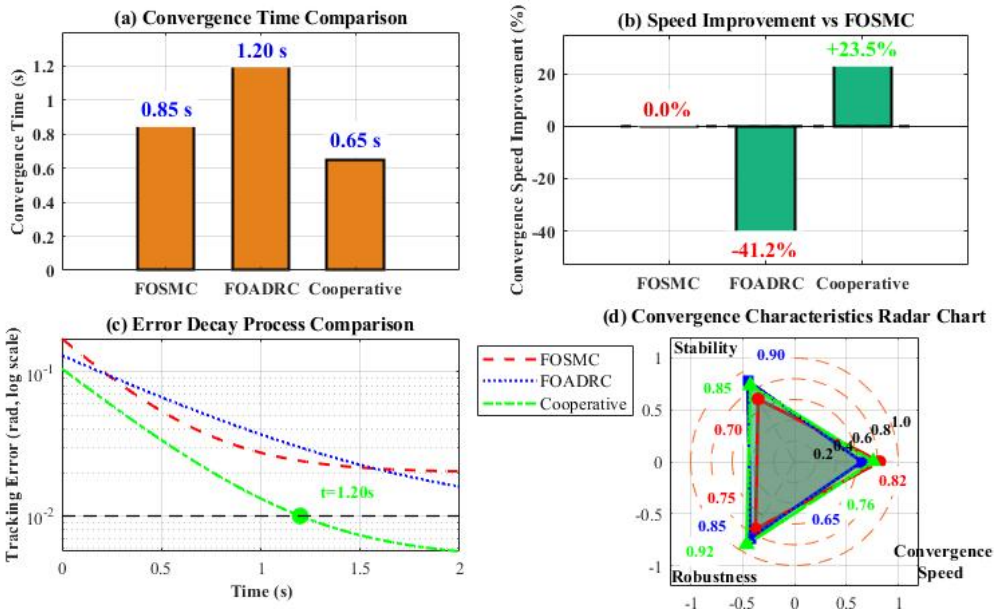


Fig.9. Comparison results of convergence speed of trajectory tracking control

Figure 9(c) shows a comparison of error attenuation processes. The error attenuation curve of FOSMC shows a rapid exponential decrease with obvious overshoot oscillation. In the initial 0.3 seconds, the error rapidly decreases but there is about 15% overshoot. The error attenuation process of FOADRC exhibits a smooth and slow exponential decline characteristic, without overshoot, but it takes a long time to converge to steady state. The error attenuation of collaborative control combines speed and smoothness, with an error attenuation of 30% of the initial value within 0.2 seconds without significant oscillation.

Figure 9(d) is a radar graph of convergence characteristics. In terms of convergence speed, FOSMC performs the best (score 0.82), followed by collaborative control (0.76), and FOADRC is relatively low (0.65). In terms of stability, FOADRC received the highest score (0.90), collaborative control was in the middle (0.85), and FOSMC was the lowest (0.70). In terms of disturbance rejection, collaborative control performs the best (0.92), followed by FOADRC (0.85), and FOSMC is relatively weak (0.75). The triangle area of the radar chart intuitively displays the comprehensive performance of each controller, and collaborative control reflects its excellent performance in three dimensions with the maximum area.

Figure 10 shows a comparison chart of control smoothness. Figure 10(a) shows the control input variance. The variance value of FOSMC is 4.5, showing obvious high-frequency oscillation characteristics. The variance of FOADRC is only 1.2, demonstrating excellent smoothing performance. The variance value of the collaborative control strategy is 2.1, reflecting its comprehensive advantage of effectively suppressing chattering while maintaining a certain response speed. The results showed that FOADRC performed the best in controlling smoothness, improving smoothness by 73.3% compared to FOSMC, while collaborative control showed a significant improvement of 53.3% compared to FOSMC.

Figure 10(b) shows the control energy consumption. The energy integration of FOSMC reaches 2850N·m·s, with relatively high energy consumption. The energy consumption of FOADRC is 1950N·m·s, with the lowest energy consumption, which is 31.6% lower than FOSMC. The energy consumption of collaborative control is 2250N·m·s, which saves 21.1% energy compared to FOSMC.

Figure 10(c) shows the control input frequency characteristics. The power spectrum of FOSMC exhibits rich high-frequency components in the 0-50Hz range, especially significant spectral energy in the 10-30Hz frequency band. The power spectrum of FOADRC is mainly concentrated in the low-frequency range of 0-10Hz, with significant attenuation of high-frequency components, reflecting its smooth control characteristics. The power spectrum distribution of collaborative control is relatively balanced, with appropriate

This article has been accepted for publication in a future issue of this journal, but has not been fully edited. Content may change prior to final publication.

spectral energy in the intermediate frequency range of 5-20Hz, which ensures sufficient bandwidth to quickly respond to dynamic changes and effectively suppresses high-frequency oscillations.

Figure 10(d) shows the percentage of smoothness improvement. The improvement percentage analysis quantified the degree of performance improvement of FOADRC and collaborative control relative to the FOSMC benchmark. FOADRC achieved a significant improvement of 73.3% in controlling variance, 31.6% in energy consumption, 53.1% in rate of change, and a comprehensive improvement degree of 52.7%. Collaborative control improved variance by 53.3%, energy consumption by 21.1%, rate of change by 37.5%, and overall improvement by 37.3%. Multi criteria evaluation shows that there is a clear trade-off relationship between different controllers in various performance indicators, and simply pursuing optimization of one indicator may lead to a decline in other performance indicators. Collaborative control achieves a reasonable balance of various performance indicators through a dynamic weight adjustment mechanism.

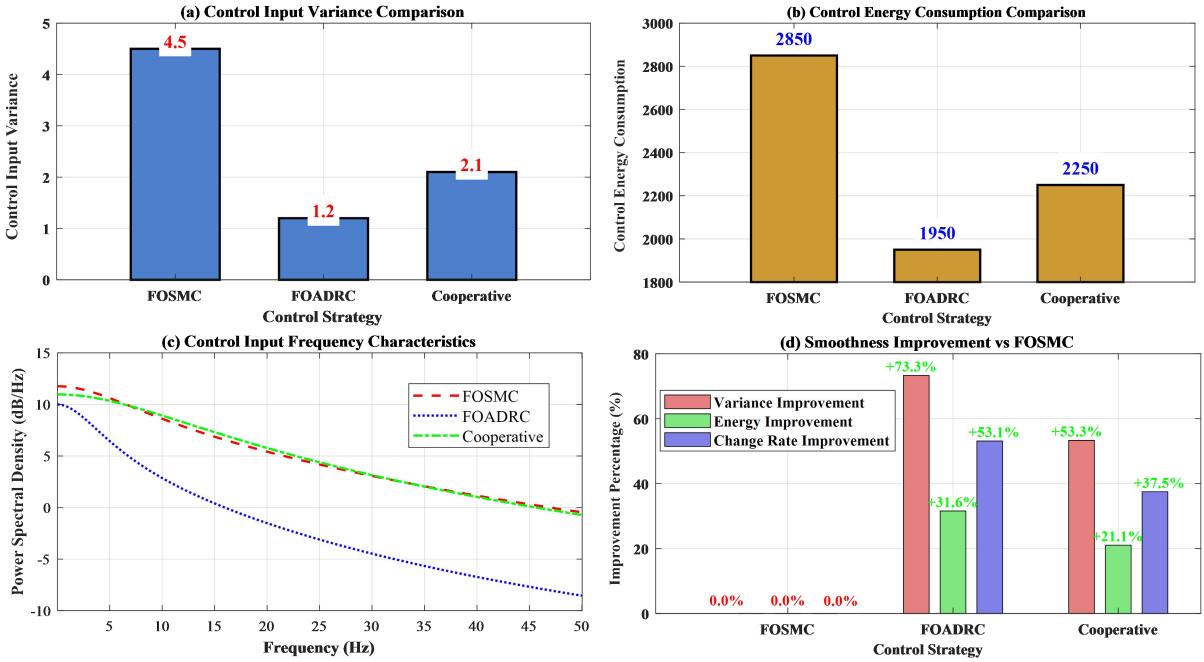


Fig.10. Comparison results of smoothness in trajectory tracking control

5. CONCLUSIONS

This paper set out to address the core challenges in high-precision manipulator control, specifically, the chattering inherent in sliding mode control, the observer bandwidth contradiction in active disturbance rejection control, the limitations of single control architectures, and the lack of dynamic collaborative mechanisms. To tackle these, a dynamic collaborative control strategy based on FOSMC and FOADRC was proposed.

The main conclusive works are summarized as follows:

(1) To suppress chattering while ensuring finite-time convergence, a fast terminal sliding mode surface integrating fractional-order integration was designed, and a switching law was formulated using the super-twisting algorithm. This directly mitigates the high-frequency chattering problem of traditional SMC.

(2) To overcome the ADRC bandwidth contradiction and improve disturbance estimation, a fractional-order LESO was designed. The PSO algorithm was introduced to automatically optimize its fractional-order PD parameters and bandwidth. This systematically reduces reliance on accurate models and resolves the trade-off between noise amplification and compensation lag.

(3) To break through the limitations of static or open-loop collaboration, a dynamic weight coordination mechanism based on an S-shaped function was proposed. By smoothly and continuously adjusting the fusion weights of FOSMC and FOADRC outputs based on real-time joint tracking error, the strategy leverages FOSMC for rapid large-error convergence and FOADRC for high-precision steady-state tracking. This directly fulfills the periodic dynamic requirements of trajectory tracking tasks.

(4) Simulation results on a two-degree-of-freedom manipulator validated the effectiveness of this approach. Compared to single controllers, the collaborative strategy reduced RMSE by over 52%, increased convergence speed by approximately 23.5%, and enhanced control smoothness with a variance reduction of over 53%. Together with theoretical robustness analysis and parameter sensitivity studies, these quantitative improvements demonstrate that the difficult problem of balancing rapid response, high accuracy, and strong robustness under model uncertainties and external disturbances has been effectively solved.

The proposed collaborative control strategy shows potential for high-precision applications such as precision assembly, surgical robots, and space manipulators, where strong robustness against uncertainties is crucial. Future work will focus on experimental validation with a physical manipulator

This article has been accepted for publication in a future issue of this journal, but has not been fully edited. Content may change prior to final publication.

and extending the dynamic coordination mechanism to multi-degree-of-freedom or multi-robot systems.

ACKNOWLEDGEMENTS

This work was supported by Natural Science Foundation of the Jiangsu Higher Education Institutions of China (No. 24KJA460009), Suzhou Key Industry Technology Innovation-Prospective Application Research Project (No. SYG202128), Jiangsu Province 3C Product Intelligent Manufacturing Engineering Technology Research and Development Center Funding Project (No. 201801000010).

REFERENCES

[1] A. Orthey, C. Chamzas, and L.E. Kavraki, "Sampling-based motion planning: A comparative review," *Annu. Rev. Control. Robot. Auton. Syst.*, vol. 7, pp. 285-310, 2023, doi: 10.1146/annurev-control-061623-094742.

[2] I. Batkovic, M. Ali, P. Falcone, and M. Zanon, "Safe trajectory tracking in uncertain environments," *IEEE Trans. Autom. Control*, vol. 68, pp. 4204–4217, 2022, doi: 10.1109/TAC.2022.3207875

[3] A.T.E. Benyahia, M. Stanković, R. Madonski, O. Babayomi and S.M. Manojlović, "Improving control performance by cascading observers: case of ADRC With cascade ESO," *IEEE/CAA Journal of Automatica Sinica,* vol. 12, no. 8, pp. 1702-1712, doi: 10.1109/JAS.2024.124995.

[4] X. Li, X. Gao, and K. Zhang, "Safe trajectory tracking for robotic manipulator with prescribed performance in confined spaces," *Symmetry*, vol. 18, pp. 2, 2026, doi: 10.3390/sym18010002

[5] T. Jin, H. Zhu, J. Zhu, S. Zhu, Z. He, S. Zhang, W. Song, and J. Gu, "Whole-body inverse kinematics and operation-oriented motion planning for robot mobile manipulation," *IEEE Trans. Ind. Inform.*, vol. 20, pp. 14239-14248, 2024, doi: 10.1109/TII.2024.3441661

[6] Z. Hu, Z. Pu, W. Xu, W. Li, and D. Meng, "Coordinated collision-free trajectory planning for a discrete-serpentine heterogeneous dual-arm space robot based on equivalent kinematics," *Aerospace*, vol. 13, pp. 34, 2026, doi: 10.3390/aerospace13010034

[7] A.T.E. Benyahia, R. Madonski, M. Stanković, S.B. Amokrane, R. Fareh, and K. Łakomy, "Fractional extended state observer for balancing noise suppression and disturbance rejection: Theoretical analysis with numerical validation," *Asian J. Control.* pp. 1-11, 2026, doi: org/10.1002/asjc.70103

[8] Z. Nie, Y. Ma, R. Liu, and D. Guo, "Improved disturbance rejection control for piezoelectric actuators based on combination of ESO and Q-filter," *Electron. Lett.*, vol. 54, pp. 872-874, 2018, doi:org/10.1049/el.2018.0909

[9] T. Liu, T. Yang, W. Xu, G. Mylonas, and B. Liang, "Efficient inverse kinematics and planning of a hybrid active and passive cable-driven segmented manipulator," *IEEE Trans. Syst. Man Cybern. Syst.*, vol. 52, pp. 4233-4246, 2022, doi: 10.1109/TSMC.2021.3095152

[10] R. Krecht, and Á. Ballagi, "Curvature-constrained motion planning method for differential-drive mobile robot platforms," *Appl. Sci.*, vol. 16, pp. 322, 2026, doi:10.3390/app16010322

[11] Z. Chen, H. Shao, B. Liu, S. Qiao, Y. Zhou, and Y. Li, "FDSPC: fast and direct smooth motion planning via continuous curvature integration," *IEEE Robot. Autom. Lett.*, vol. 10, pp. 10878-10885, 2025, doi: 10.1109/LRA.2025.3604729

[12] F. Ye, F. Le, L. Cui, S. Han, J. Gao, J. Qu, and X. Xue, "Application of Navigation Path Planning and Trajectory Tracking Control Methods for Agricultural Robots," *Agriculture*, vol. 16, pp. 64, 2026, doi: 10.3390/agriculture16010064

[13] J. Zhao, J. Dong, P.K. Wong, J. Liu, T.H. Pang, Z. Yang, X. Ma, and Z. Xie, "Random multiphysics measurement for electro-hydraulic system with hysteresis diagnosis," *IEEE Trans. Instrum. Meas.*, vol. 74, pp. 1002214, 2025, doi: 10.1109/TIM.2025.3529051

[14] M. Stankovic, T. He, and R. Madonski, "From PID to ADRC and back: Expressing error-based active disturbance rejection control schemes as standard industrial 1DOF and 2DOF controllers," *Asian J. Control*., vol. 26, pp. 2796-2806, 2024, doi: 10.1002/asjc.3373.

[15] H. Wang, K. Xu, and H. Zhang, "Adaptive finite-time tracking control of nonlinear systems with dynamics uncertainties," *IEEE Trans. Autom. Control*, vol. 68, pp. 5737-5744, 2022, doi: 10.1109/TAC.2022.3226703

[16] X. Liang, K. Jiang, W. Gao, and B. Yao, "Research on a force-sensorless control method for an agricultural manipulator based on fuzzy sliding mode control and a disturbance observer," *Agronomy*, vol. 16, pp. 1940, 2026, doi: org/10.3390/agronomy16191940

[17] B. Li, S. Wen, Z. Yan, G. Wen, and T. Huang, "A survey on the control lyapunov function and control barrier function for nonlinear-affine control systems," *IEEE/CAA J. Autom. Sin.*, vol. 10, pp. 584-602, 2023, doi:10.1109/JAS.2023.123075

[18] X. Zhang, G. Li, F. Xiao, D. Jiang, B. Tao, J. Kong, G. Jiang, and Y. Liu, "An inverse kinematics framework of mobile manipulator based on unique domain constraint," *Mech. Mach. Theory*, vol. 183, pp. 105273, 2023, doi: 10.1016/j.mechmachtheory.2023.105273

[19] C. Li, F. Liu, Y. Wang, and M. Buss, "Concurrent learning-based adaptive control of an uncertain robot manipulator with guaranteed safety and performance," *IEEE Trans. Syst. Man Cybern. Syst.*, vol. 52, pp. 3299-3313, 2021, doi: 10.1109/TSMC.2021.3064971

[20] Y. Sun, J. Liu, Y. Gao, Z. Liu, and Y. Zhao, "Adaptive neural tracking control for manipulators with prescribed performance under input saturation," *IEEE/ASME Trans. Mechatronics*, vol. 28, pp. 1037-1046, 2022, doi: 10.1109/TMECH.2022.3213441

[21] S. Baek, J. Baek, W. Kwon, and S. Han, "An adaptive model uncertainty estimator using delayed state-based model-free control and its application to robot manipulators," *IEEE/ASME Trans. Mechatron.*, vol. 27, pp. 4573-4584, 2022, doi: 10.1109/TMECH.2022.3160495

[22] R. Chai, H. Niu, J. Carrasco, F. Arvin, H. Yin, and B. Lennox, "Design and experimental validation of deep reinforcement learning-based fast trajectory planning and control for mobile robot in unknown environment," *IEEE Trans. Neural Netw. Learn. Syst.*, vol. 35, pp. 5778-5792, 2024, doi: 10.1109/TNNLS.2022.3209154

[23] X. Li, L. Luo, H. Zhao, D. Ge, and H. Ding, "Inverse kinematics solution based on redundancy modeling and desired behaviors optimization for dual mobile manipulators," *J. Intell. Robot. Syst.*, vol. 108, pp. 37, 2023, doi: 10.1007/s10846-023-01884-5

[24] L. Zhang, Y. Su, Z. Wang, and H. Wang, "Fixed-time terminal sliding mode control for uncertain robot manipulators," *ISA Trans.*, vol. 144, pp, 364-373, 2024, doi: 10.1016/j.isatra.2023.10.011

[25] G. Sun, Q. Liu, F. Pan, and J. Zheng, "Disturbance observer based adaptive predefined-time sliding mode control for robot manipulators with uncertainties and disturbances," *Int. J. Robust Nonlinear Control*, vol. 34, no. 18, pp. 12349-12374, 2024, doi: 10.1002/rnc.7628

[26] N. Wagaa, H. Kallel, and N. Mellouli, "Analytical and deep learning approaches for solving the inverse kinematic problem of a high degrees of freedom robotic arm," *Eng. Appl. Artif. Intell.*, vol. 123, pp. 106301, 2023, doi: 10.1016/j.engappai.2023.106301

This article has been accepted for publication in a future issue of this journal, but has not been fully edited. Content may change prior to final publication.